Supplementary Information

for

Boron fused pyrazolyl zinc salen as a self-powered ultra-Sensitive sensor for pico-molar nicotine detection in realistic smoke environments

Sasmita Dhala,[a‡] Prakash Nayak,[a‡] Indrajit Mondal,[b‡] Chinmaya Sahoo[b], Satyaprasad P. Senanayak*[b,c] Krishnan Venkatasubbaiah,*[a,c]
[a]School of Chemical Sciences, National Institute of Science Education and Research (NISER), an OCC of Homi Bhabha National Institute, Bhubaneswar-752050, Odisha, India. E-mail: krishv@niser.ac.in
[b]School of Physical Sciences, National Institute of Science Education and Research (NISER), an OCC of Homi Bhabha National Institute, Bhubaneswar-752050, Odisha, India, E-mail: satyaprasad@niser.ac.in
[c]Centre for Interdiscsiplinary Sciences, National Institute of Science Education and Research, Bhubaneswar, Odhisha, 752050, India.

[‡]equal contribution

Table of Content

1. General information

All reagents were used as received from Spectrochem, Alfa-Aesar and Sigma-Aldrich unless otherwise noted. Dichloromethane and toluene were dried using calcium hydride and Na/benzophenone respectively. The substrates and complexes were characterized by multinuclear NMR data. All ^{1}H (400 MHz), ^{13}C (100 MHz), and ^{11}B (128 MHz) NMR were recorded at room temperature on Bruker ARX 400 MHz spectrometer. Residual protonated solvents were used as internal standards for ^{1}H and ^{13}C NMR. ^{11}B NMR spectra were referenced externally to $BF_3{\cdot}Et_2O$ in $CDCl_3$ (δ = 0 ppm). ESI mass spectra were recorded with Bruker micro TOF-QII mass spectrometer. Elemental analyses of the compounds were performed using a Euro Vector EA instrument (CHNS-O, model EuroEA3000). Rigaku Oxford X-ray diffractometer having Cu-Kα radiation (1.54184 Å) and Mo-Kα radiation (0.71073 Å) was used for collecting single crystal X-ray diffraction data. SADABS absorption corrections were applied. Olex were used for structure solving and refinement. Anisotropic refinements were used for non-hydrogen atoms. The H atoms were placed at calculated positions and were refined as riding atoms (CCDC no. 2519213-2519214). UV-Visible spectra were recorded on JASCO V-730 UV/Visible spectrometer. The fluorescence spectra were recorded with a Edinburgh Instruments FS5 Spectrofluorometer.

2. Synthesis and analytical data

Synthesis of compound TPZBSA: To 150 ml two neck RB, compound **TPZB** (1.09 mmol, 0.5 g, 2 equiv.) and *trans*-1,2-diaminocyclohexane (0.55 mmol, 66 µL, 1 equiv.) were added to dry methanol and refluxed overnight under nitrogen. The reaction mixture was filtered and a yellow precipitate of compound **5** was collected. Yield: 88% (544 mg) ^{1}H NMR (400 MHz, DMSO-d_6): δ = 13.39 (s, 2H), 8.58 (s, 2H), 7.89 (d, *J* = 8.0, 4H), 7.76 (d, *J* = 8.0 Hz, 4H), 7.70 – 7.62 (m, 9H), 7.61 – 7.42 (m, 11H), 7.18 – 7.10 (m, 4H), 6.84 (d, *J* = 8.0 Hz, 4H), 6.69 (d, *J* = 8.0 Hz, 2H), 3.46 – 3.39 (m, 2H), 1.91 (m, 2H), 1.81 (m, 2H), 1.65 (m, 2H), 1.48 (m, 2H), 0.06 (s, 12H). ^{13}C NMR (101 MHz, DMSO-d_6) δ 165.38, 159.90, 155.79, 147.98, 140.13, 137.51, 136.84, 130.77, 130.52, 129.65, 129.15, 128.91, 128.55, 127.95, 126.67, 123.08, 118.63, 116.87, 111.55, 111.27, 71.27, 32.43, 23.70, 9.68 ppm. HRMS (ESI+, m/z) calcd for $C_{66}H_{61}B_2N_6O_2$, $[M+H]^+$ m/z = 991.5056, found = 991.5000.

Synthesis of complex TPZBSA-Zn: To 150 mL two neck RB, compound **TPZBSA** (300 mg, 0.3 mmol, 1 equiv.) was dissolved in 15 mL DCM and a solution of $Zn(OAc)_2.2H_2O$ (72 mg, 0.33 mmol, 1.1 equiv.)

in 15 mL methanol was added dropwise under nitrogen. The greenish-yellow solution was refluxed for 12 h. Light green color crystals of complex **TPZBSA-Zn** with a coordinated DMSO molecule were collected in DMSO/Methanol solvent system after 1 week. Yield: 68% (215 mg) ^{1}H NMR (400 MHz, DMSO-d_6) δ 8.48 (s, 2H), 7.90 (d, *J* = 8.0 Hz, 2H), 7.82 – 7.73 (m, 4H), 7.71 – 7.63 (m, 7H), 7.61 – 7.50 (m, 8H), 7.47 (d, *J* = 8.0 Hz, 2H), 7.20 (d, *J* = 8.0 Hz, 2H), 7.11 (s, 2H), 6.70 (d, J = 8.0 Hz, 4H), 3.26 – 3.16 (m, 2H), 1.97 – 1.86 (m, 2H), 1.44 – 1.39 (m, 2H), 1.28 – 1.27 (m, 2H), 0.89 – 0.73 (m, 2H), 0.09 (s, 12H). ^{13}C NMR (101 MHz, DMSO-d_6) δ 170.43, 165.17, 147.80, 139.88, 138.49, 135.97, 133.28, 131.06, 130.52, 129.70, 129.17, 129.02, 128.56, 128.07, 125.73, 124.05, 123.12, 122.11, 119.33, 111.52, 111.12, 64.66, 27.78, 23.85, 22.34, 9.81. ^{11}B-NMR (128 MHz, DMSO-d_6) δ -2.24 MALDI-MS calcd for $C_{66}H_{58}B_2N_6O_2Zn$, $[M]^+$ m/z = 1054.2, found 1054.4. Anal. Calcd for $C_{66}H_{58}B_2N_6O_2Zn$: C, 75.19; H, 5.55; N, 7.97. Found: C, 74.91; H, 5.89; N, 8.72.

3. Photophysical studies of complex along with nicotine detection

Table S1: Photophysical data of complex **TPZBSA-Zn**

Solvent	**λ_{max} (nm)**	**ε x 10^4 (mol^{-1} L cm^{-1})**	**λ_{ems}[a] (nm)**	**ΔE (cm^{-1}) Stokes shift**	**Absolute QY[b] (ϕ)**
THF	379	10.34	475	5332.59	13.29 %

[a]excited at absorption maxima, [b]absolute quantum yield using integrating sphere.

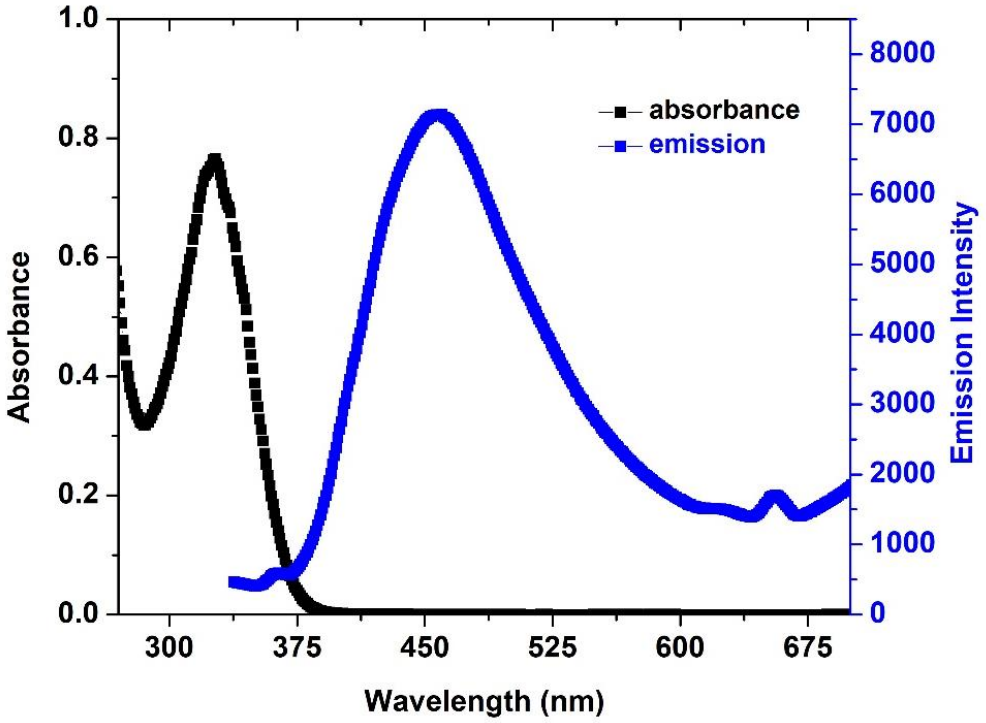

Figure S1: Absorption and emission spectra of compound **TPZBSA-Zn** in THF at 1 x 10^{-5} M concentration.

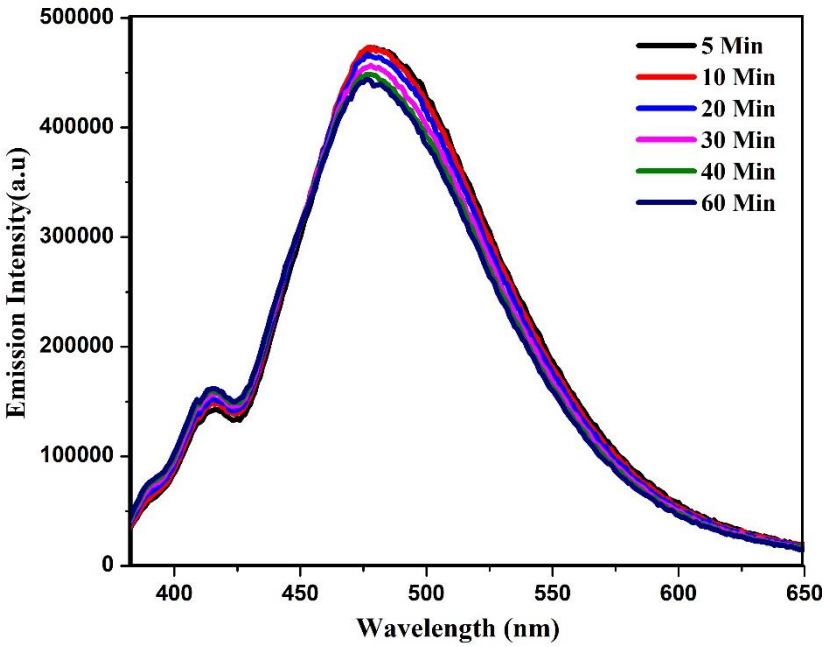

Figure S2: Time-dependent fluorescence emission spectra of **TPZBSA-Zn** (1×10^{-5} M in $CHCl_3$) recorded over 60 minutes at 5–10 minute intervals.

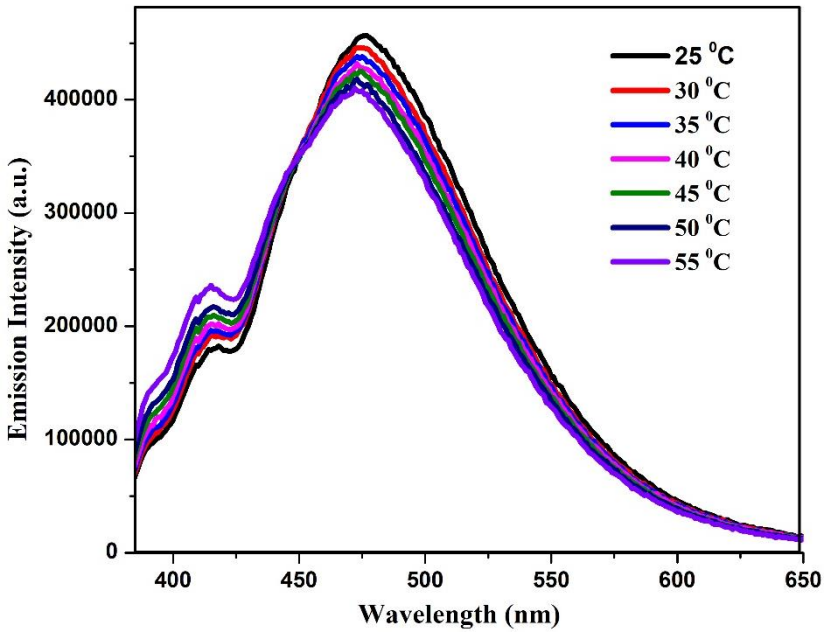

Figure S3: Temperature-dependent fluorescence emission of **TPZBSA-Zn** (25–55 °C).

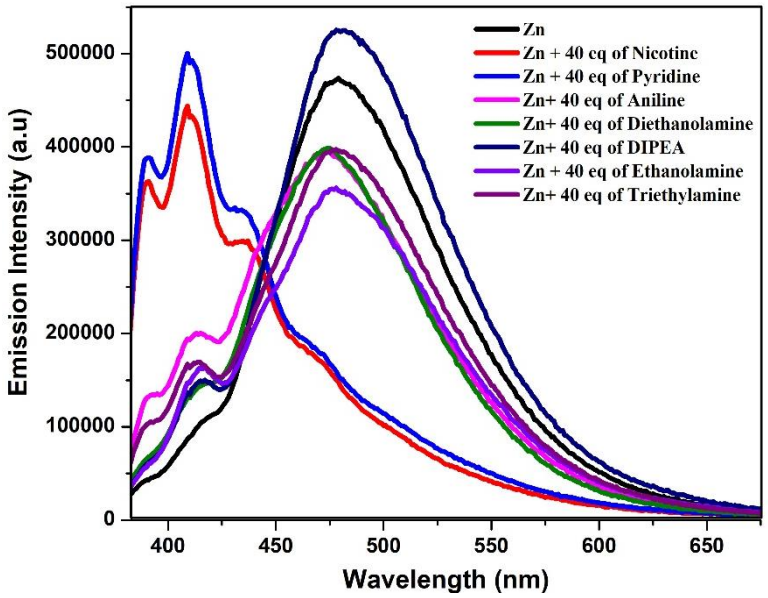

Figure S4: Selectivity of **TPZBSA-Zn** towards nicotine in the presence of various amines (40 equivalents).

Detection limit calculation:

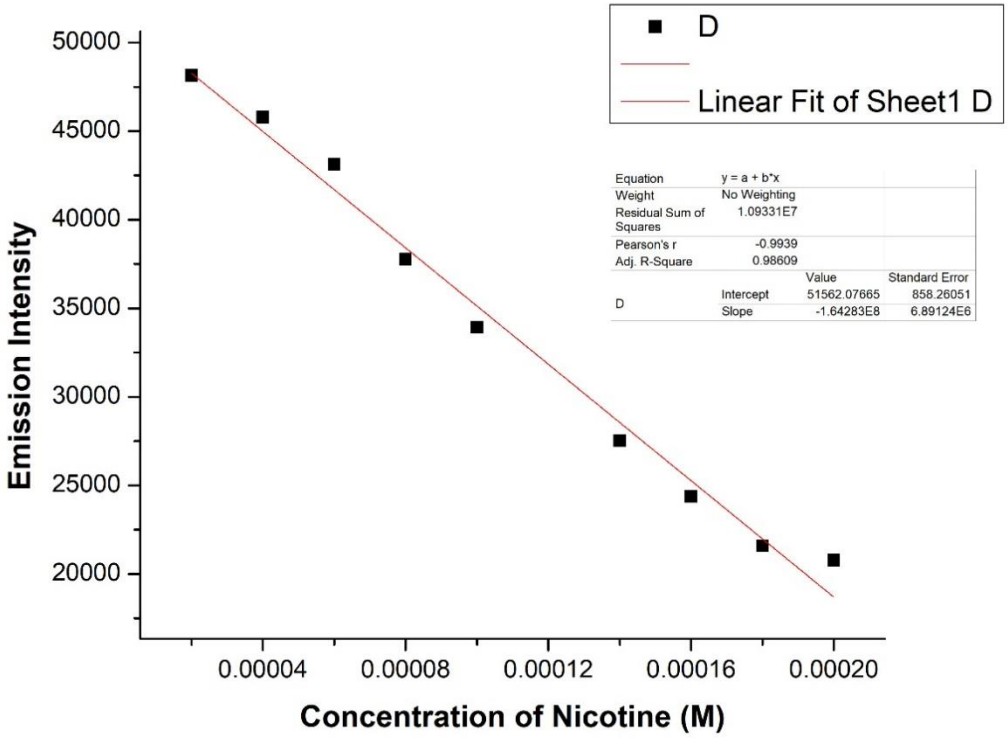

Figure S5: Detection limit of compound **TPZBSA-Zn** towards Nicotine (2 – 20 equivalences) in $CHCl_3$ at **480nm**.

Calculation of detection limit:

Detection Limit = 3ρ/K**,** ρ = Standard deviation of blank measurement.

K = Slope between the fluorescence intensity *Vs* nicotine concentration.

Standard deviation = 76.62

Slope = $-1.64 \times 10^8\ M^{-1}$ at 480nm

Detection Limit = 1.4 μM

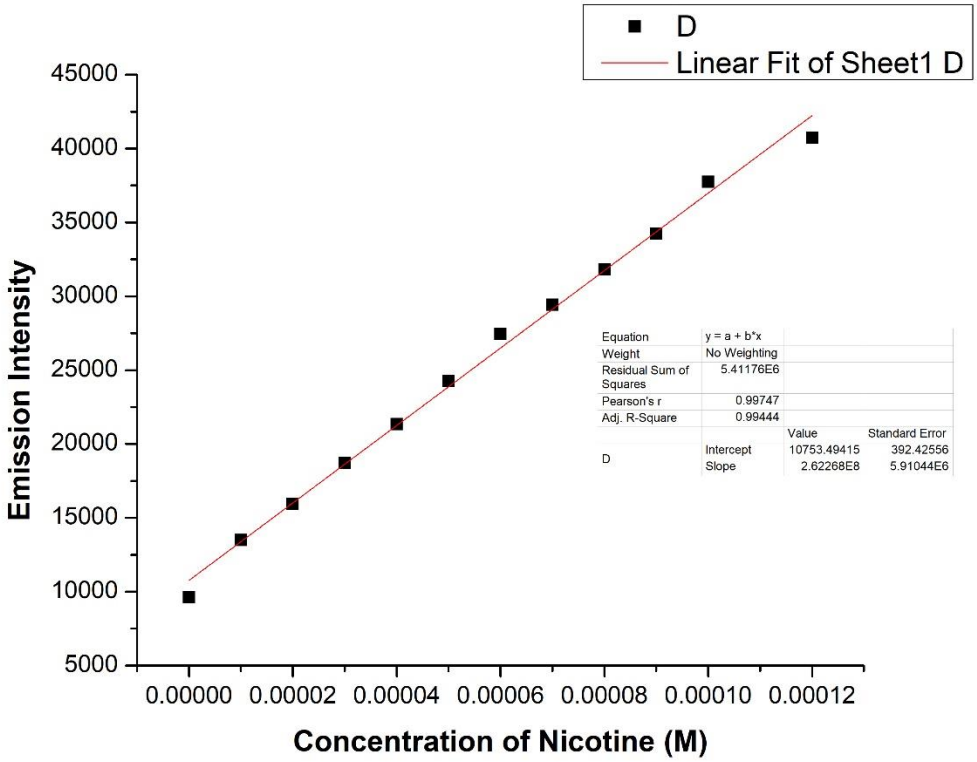

Figure S6: Detection limit of compound **TPZBSA-Zn** towards Nicotine (0 – 20 equivalences) in $CHCl_3$ at **408nm**.

Standard deviation = 76.62

Slope = $2.62 \times 10^8\ M^{-1}$ at 408nm

Detection Limit= 0.87 µM**.**

Test strip Detection:

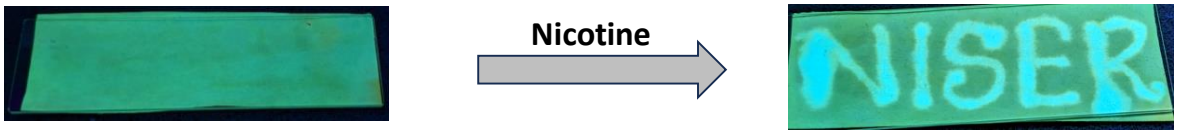

Figure S7: Test strip detection using compound **TPZBSA-Zn**.

4. NMR titration:

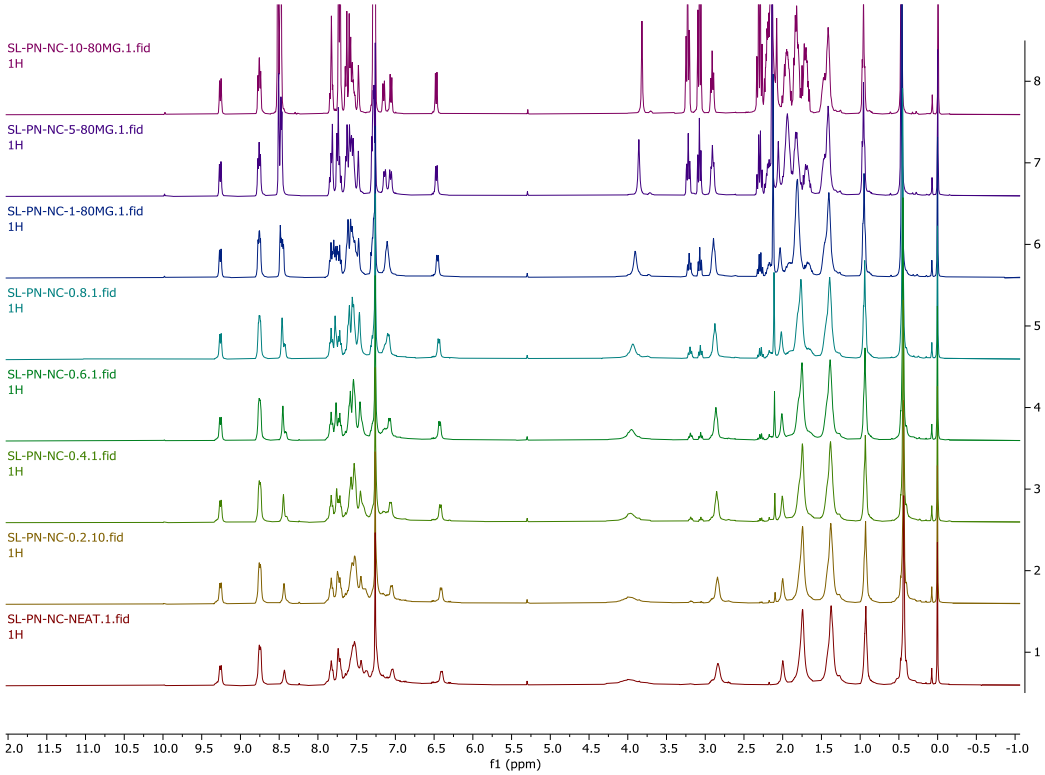

Figure S8: Stacked image of NMR titration of **TPZBSA-Zn** with nicotine in **$CDCl_3$**.

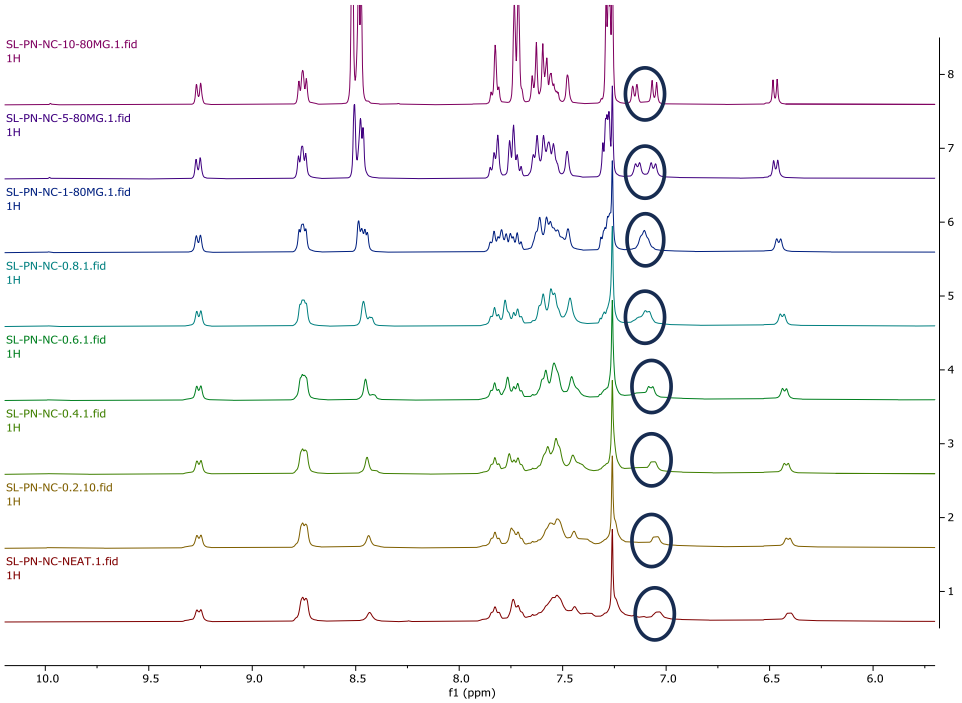

Figure S9: Staked image of nmr titrations of aromatic region of **TPZBSA-Zn** with nicotine in $CDCl_3$.

5. X-ray data for DMSO and nicotine-complexes

Table S2: Crystal Data and structure refinement for complex **TPZBSA-Zn-DMSO** and **TPZBSA-Zn -nicotine**

	TPZBSA-Zn-DMSO	**TPZBSA-Zn-nicotine**
Empirical formula	$C_{68}H_{64}B_2N_6O_3SZn$	$C_{76}H_{72}B_2N_8O_2Zn$
Formula weight	1132.30	1216.40
Temperature/K	100.00(10)	100.00(10)
Crystal system	monoclinic	triclinic
Space group	$P2_1/c$	P-1
a/Å	10.5921(5)	12.9589(4)
b/Å	25.3125(8)	14.4323(4)
c/Å	23.2577(10)	19.4451(5)
α/°	90	98.237(2)
β/°	95.528(4)	107.421(2)
γ/°	90	109.381(3)
Volume/$Å^3$	6206.7(4)	3152.14(17)
Z	4	2
$\rho_{calc}g/cm^3$	1.212	1.282
μ/mm^{-1}	0.480	0.445
F(000)	2376.0	1280.0
Crystal size/mm^3	0.18 × 0.15 × 0.13	0.16 × 0.14 × 0.12
Radiation	MoKα (λ = 0.71073)	MoKα (λ = 0.71073)
2Θ range for data collection/°	6.44 to 59.116	6.772 to 60.802
Index ranges	$-12 \le h \le 13$, $-31 \le k \le 30$, $-31 \le l \le 29$	$-15 \le h \le 17$, $-19 \le k \le 20$, $-27 \le l \le 25$
Reflections collected	65184	57581
Independent reflections	14140 [R_{int} = 0.0886, R_{sigma} = 0.0783]	15259 [R_{int} = 0.0515, R_{sigma} = 0.0519]
Data/restraints/parameters	14140/1007/765	15259/155/807
Goodness-of-fit on F^2	1.043	1.054
Final R indexes [I>=2σ (I)]	R_1 = 0.1188, wR_2 = 0.2953	R_1 = 0.0819, wR_2 = 0.2044
Final R indexes [all data]	R_1 = 0.1671, wR_2 = 0.3279	R_1 = 0.1068, wR_2 = 0.2179
Largest diff. peak/hole / e $Å^{-3}$	2.36/-1.75	2.26/-0.97

Table S3: Selected bond lengths and bond angles of complex **TPZBSA-Zn-DMSO**.

	Bond lengths (Å)		**Bond Angles (°)**
Zn1-O1	1.969(5)	O1-Zn1-N4	152.8(3)
Zn1-O2	1.980(4)	O1-Zn1-O3	98.1(3)
Zn1-O3	2.029(5)	O1-Zn1-N3	89.0(2)
Zn1-N4	2.081(5)	O3-Zn1-N4	108.3(3)
Zn1-N3	2.073(5)	O3-Zn1-N3	105.4(2)
B1-N6	1.649(8)	N3-Zn1-N4	78.1(2)
B1-C15	1.619(10)	C12-B1-N6	94.6(4)
B1-C14	1.605(10)	C12-B1-C14	115.2(6)
B1-C12	1.586(7)	C12-B1-C15	113.3(5)
B2-C44	1.603(10)	C14-B1-N6	112.4(5)
B2-C45	1.612(10)	C14-B1-C15	113.0(5)
B2-C40	1.613(9)	C15-B1-N6	106.6(5)
B2-N1	1.669(8)	C40-B2-N1	94.6(5)
	Bond Angles (°)	C45-B2-N1	112.8(5)
O2-Zn1-N4	89.67(18)	C45-B2-C40	110.3(5)
O2-Zn1-O3	98.1(2)	C44-B2-N1	109.5(5)
O2-Zn1-N3	156.0(2)	C44-B2-C40	114.7(6)
O1-Zn1-O2	93.0(19)	C44-B2-C45	113.5(6)

Table S4: Selected bond lengths and bond angles of **TPZBSA-Zn-nicotine**.

	Bond lengths (Å)		**Bond Angles (°)**
Zn1-O1	1.971(3)	O1-Zn1-N3	107.65(12)
Zn1-O2	1.975(3)	O1-Zn1-N1	141.58(14)
Zn1-N3	2.124(3)	O1-Zn1-N2	88.63(12)
Zn1-N1	2.106(3)	N1-Zn1-N3	108.98(13)
Zn1-N2	2.101(3)	N2-Zn1-N3	93.45(12)
B1-N6	1.664(6)	N2-Zn1-N1	78.07(12)
B1-C14	1.612(6)	C14-B1-N6	94.9(3)
B1-C20	1.614(7)	C14-B1-C20	112.4(4)
B1-C21	1.623(7)	C14-B1-C21	110.5(4)
B2-C60	1.621(5)	C20-B1-N6	109.6(4)
B2-C61	1.609(5)	C20-B1-C21	115.4(4)
B2-C56	1.611(5)	C21-B1-N6	112.2(4)
B2-N8	1.638(5)	C61-B2-N8	111.2(3)
	Bond Angles (°)	C61-B2-C56	113.6(3)
O2-Zn1-N3	96.42(11)	C61-B2-C60	114.9(3)
O2-Zn1-N1	89.39(11)	C56-B2-N8	94.7(2)
O2-Zn1-N2	166.05(11)	C56-B2-C60	113.1(3)
O1-Zn1-O2	97.70(11)	C60-B2-N8	107.4(3)

Table S5: Comparison of previously reported nicotine detection methods with the present **TPZBSA-Zn**.

SL No.	Detection Method	Sensing Probe	Detection limit	Advantages	Limitations	References
1	Electrochemical sensing	Graphene oxide modified glassy carbon electrode	12.7 nM	Good selectivity and reproducibility	Complicated electrochemical setup and electrode modifications	[1]
2	Electrochemical Sensing	Cerium nanoparticles with anionic surfactants	9.43 x 10^{-8} M	Applicable to real cigarette samples	Requires electrode preparation and buffer preparation	[2]
3	Graphene-based electrochemical Sensing	Graphene oxide-supported gold nanoparticles	0.015 µM	Wide detection range	Needs complex nano-composite fabrication	[3]
4	Fluorescence and electrochemical sensing	MOF-based dual sensor	0.25 µM	Dual sensing capability	Relatively higher detection limit	[4]
5	Electrochemilu-minescence	Gold nanocluster	7.0 x 10^{-13} M	Very high sensitivity	Requires complex ECL instrumentation	[5]
6	Electrochemical Sensing	Multi-walled carbon nanotube	1.42 µM	Enhanced sensitivity and lower oxidation potential	Complex electrode fabrication and setup	[6]
7	Gasochromic Sensing	Metal-Organic nanotube	23.3 µM	Simple visual detection, No complex instrumentation	Lower sensitivity, limited to vapour phase	[7]
8	Spectrophotometric method	Plasmonic Nanoparticles	0.001-0.090 µM	Simple and cost-effective	Lower sensitivity	[8]

9	Spectrophotometric method	MIP/ZnO nanostructure-based electrode	2.0 $\times 10^{-9}$M	High selectivity	Complex fabrication	[9]
10	Electrochemical sensing	BN-doped graphene film modified electrode	0.42 µM	Good electrocatalytic activity and selectivity	Requires device fabrication	[10]
11	Electrochemical	Nanocomposite-modified electrode	0.02637 µM	High sensitivity, cost-effective,	Stability issues	[11]
12	Electrochemical	Ag-nanoparticles	0.135 µM	Good selectivity	Limited linear range	[12]
13	HPLC	Reverse-phase C18 column	-	Well-established method	Sample preparation, time consuming	[13]
14	Fluorometric and conductometric Method	Boron-functionalized Zn-salen complex device (TPZBSA-Zn)	1.0 x 10^{-12} M	Dual fluorescence and conductomtric sensing, ultra-low detection limit, detection in vapor and liquid phases, applicable to real cigarette smoke	-	**This Work**

5. Device fabrication and Characterizations

For the device fabrication glass substrates were cleaned sequentially ultrasonicating in soap solution, DI water, Acetone and isopropanol (IPA) for 10 minutes each. The cleaned substrates were then treated in a UV-ozone chamber for 15 minutes to render the surface hydrophilic and to remove residual organic contaminants through oxidative volatilization. Cr/Au electrode (5 nm/20 nm) were then deposited through a suitable physical mask to realize a channel dimension L = 100 µm, W = 1mm. Subsequently, a 10 mg/mL solution of the **TPZBSA-Zn** complex was prepared in tetrahydrofuran (THF), and 60 µL of this solution was spin-coated onto the gold-coated substrates at 1000 rpm for 60 seconds, resulting in a uniform thin film suitable for device fabrication.

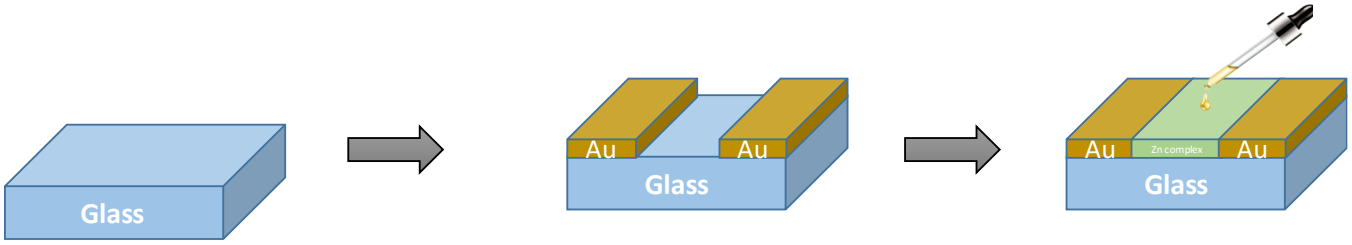

Figure S10: Stepwise schematic illustration of the **TPZBSA-Zn** complex device fabrication process.

a) *Liquid nicotine exposure:* Typical conductivity variation of the sensor along with the schematic of the sensing procedure is plotted in **figure S8**.

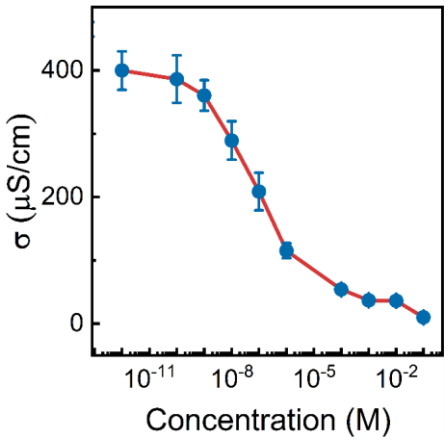

Figure S11. Plot of the device conductivity upon exposure to liquid nicotine.

Upon exposure of the **TPZBSA-Zn** complex device with nicotine vapor a clearly color change of the device is observed (**Figure S9**).

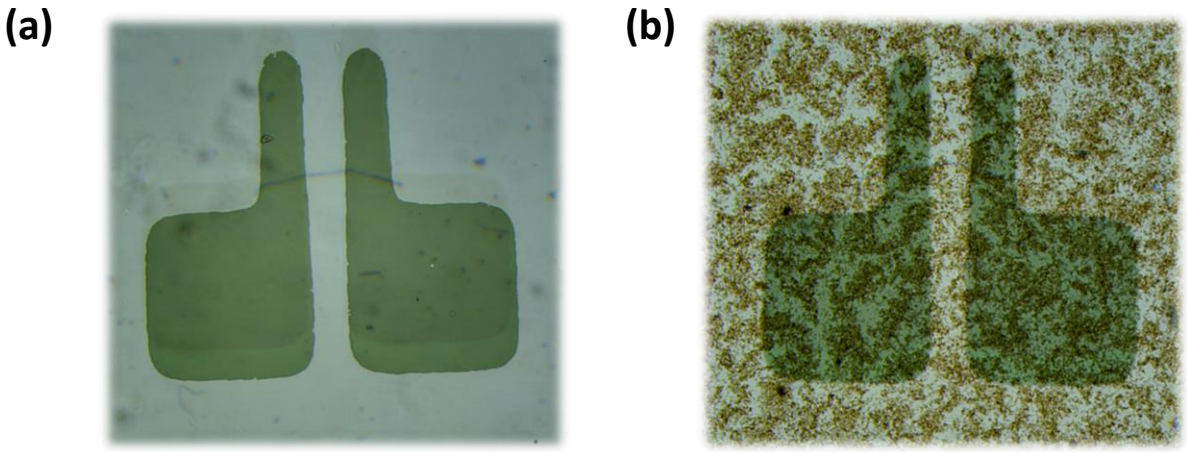

Figure S12. Optical images of the **TPZBSA-Zn** film before (left) and after (right) liquid nicotine exposure, showing noticeable changes.

To quantitatively describe the observed response of the Zn complex to liquid phase nicotine, we fitted the conductivity change using the Logistic function: $f(x) = A_2 + \frac{A_1 - A_2}{1 + (x/x_0)^k}$ where A_1 and A_2 represent the initial and final conductivity values, x_o denotes the inflection point (center of response), and k defines the slope or sharpness of the transition. The excellent agreement between the experimental data and the fitted curve confirms the reliability of the **TPZBSA-Zn** complex as an ultrasensitive and predictable nicotine detection system, capable of operating effectively across an exceptionally wide concentration range.

b) Vapour nicotine exposure: To simulate a realistic exposure environment, the **TPZBSA-Zn** complex-based device was subjected to nicotine vapour under controlled thermal conditions. The device was placed on a hot plate, and a few drops of nicotine solutions of different concentration were dispensed onto a separate glass substrate positioned adjacent to it. To facilitate gradual evaporation of nicotine, the hot plate temperature was slowly raised to 70 °C. The entire setup was then covered with a petri dish to confine the nicotine vapors and minimize ambient interference. This ensures enhanced interaction between the evaporated nicotine molecules with the **TPZBSA-Zn** complex-based device **(Figure S10).** Moreover, this allows a precise control over the concentration of nicotine to understand the reliability range of the sensing. The device was exposed to nicotine vapour for different durations initially for 30 minutes (Figure S9b) and subsequently for 60 minutes (**Figure 4d**). A pronounced decrease in electrical conductivity was observed, significantly greater than that obtained from liquid-phase nicotine exposure, confirming a stronger and more realistic interaction between the vapour-phase nicotine and the **TPZBSA-Zn** film. This enhanced response highlights the device's exceptional sensitivity and suitability for detecting gaseous nicotine in practical, real-world conditions such as tobacco smoke environments.

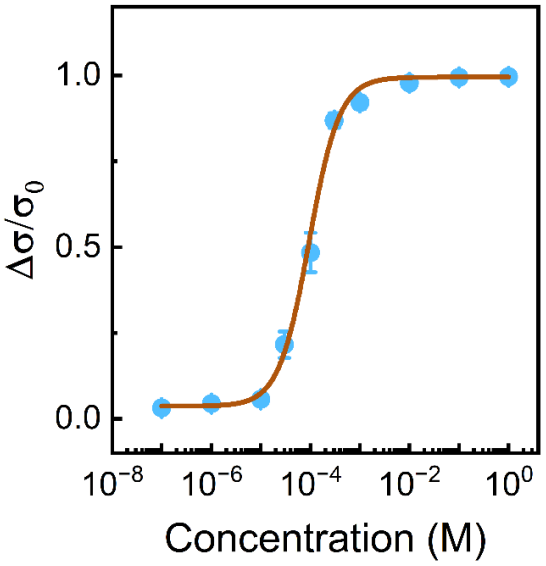

Figure S13. Relative conductivity variation of the device following exposure to nicotine vapors for 30 minutes, demonstrating its high sensitivity toward gaseous nicotine.

c) Cigarette and Bidi exposure: To further evaluate the practical applicability of the **TPZBSA-Zn** based sensing platform, real-life nicotine exposure experiments were conducted using cigarette and bidi. In this setup, puffs of cigaratte or bidi smoke (**Figure 4f, S11a**) were exposed to sensing device in a closed chamber comparable to a airplane lavatory. As a control experiment we also made multiple puffs of ambient air from human subject to the device which exhibit no significant change whereas the same device exposed to a single smoke blow exhibited a decrease in channel current by atleast 1.5 times (**Figure S11b**). The substantial current variation observed exclusively in the presence of cigarette smoke, as opposed to negligible fluctuations under ambient air, confirms that the response arises from nicotine interaction rather than environmental conditions or humidity-driven artefacts. Plot of relative conductivity variation with multiple blows/puffs of cigaratte and bidi smoke from human subject is demonstrated in **figure 11c** indicating real-time application of our device in closed chamber.

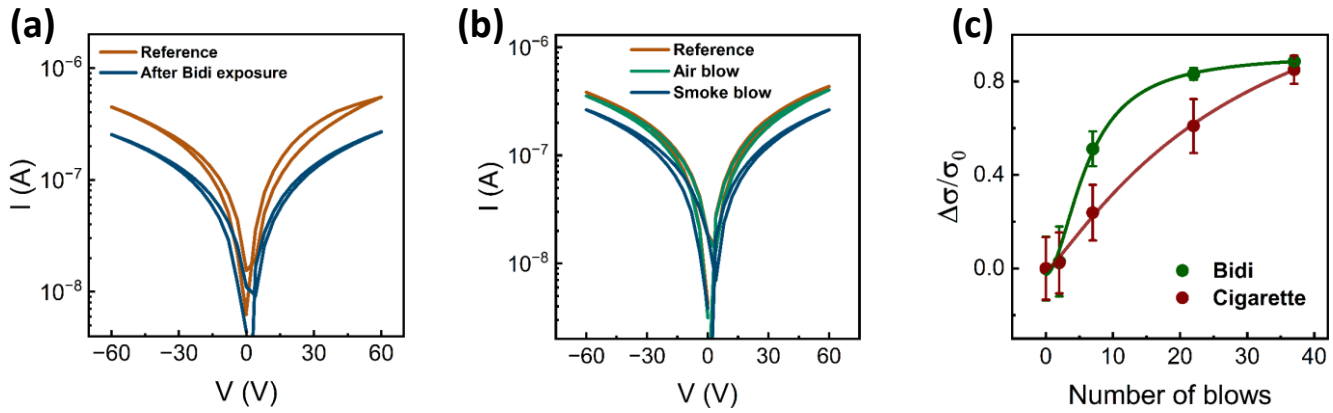

Figure S14 (a)Current response of the **TPZBSA-Zn** complex device upon exposure to bidi smoke in 45 ft^3 chamber. (b) Comparative I-V characteristics under ambient air and cigarette smoke, demonstrating nicotine-induced current modulation upon blows of smokes. (c) Relative conductivity response of the device during exposure to multiple bows/puffs of cigarette and bidi smoke from human subject.

d) Stability test and Control experiments: To evaluate the intrinsic operational stability of the **TPZBSA-Zn** device, time-dependent conductivity measurements were performed under ambient conditions. Immediately after fabrication, the device exhibited an initial conductivity of approximately 400 µS/cm, which gradually decreased over time (**Figure S15a**). This decline is attributed to slow oxidative degradation of the zinc–organic framework, driven by interactions with atmospheric oxygen and moisture. In addition, the cyclic bias stress applied during measurement (− 60 V to + 60 V) may induce trap formation or charge redistribution within the semiconductor layer, further contributing to the observed conductivity decay.

The stability behaviour was further examined under controlled nicotine vapour exposure (**Figure S15b**). The device which initially displayed a conductivity of 360 µS/cm, which decreased to 276 µS/cm upon exposure to 1 nM nicotine vapour, demonstrating strong charge-transfer interactions between nicotine molecules and the Zn-centred binding sites. Interestingly, the conductivity recovers back close to its original value (335 µS/cm) over the next 90 minutes, before gradually declining again to environmental conditons. This reversible modulation suggests that nicotine adsorption and desorption processes occur at the molecular interface, implying that the sensing layer remains reusable without requiring regeneration treatments.

The quantitative trend observed during vapour exposure was consistent with earlier controlled concentration experiments and cigarette-smoke testing, confirming the reliability and reproducibility of the response mechanism across multiple exposure environments. The stability profile also supports that the device retains measurable sensitivity even after repeated exposure cycles, and calibration throughout the study confirmed that the response is concentration-dependent and quantitatively interpretable.

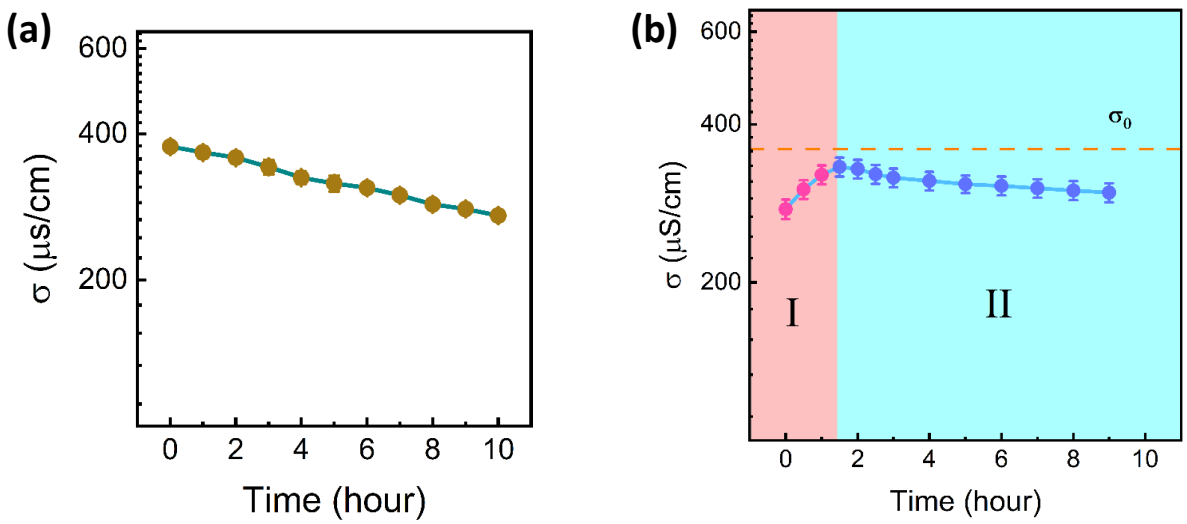

Figure S15 (a) Evolution of the device conductivity of the pristine **TPZBSA-Zn** film in ambient conditions. (b) Sensing and recovery characteristics of the nicotine-exposed TPZBSA–Zn film. Region (I) represents the recovery behavior of the device after nicotine exposure, showing the gradual return toward its initial electrical state. Region (II) illustrates the subsequent stability of the device after recovery, demonstrating its ability to maintain near-initial performance over time.

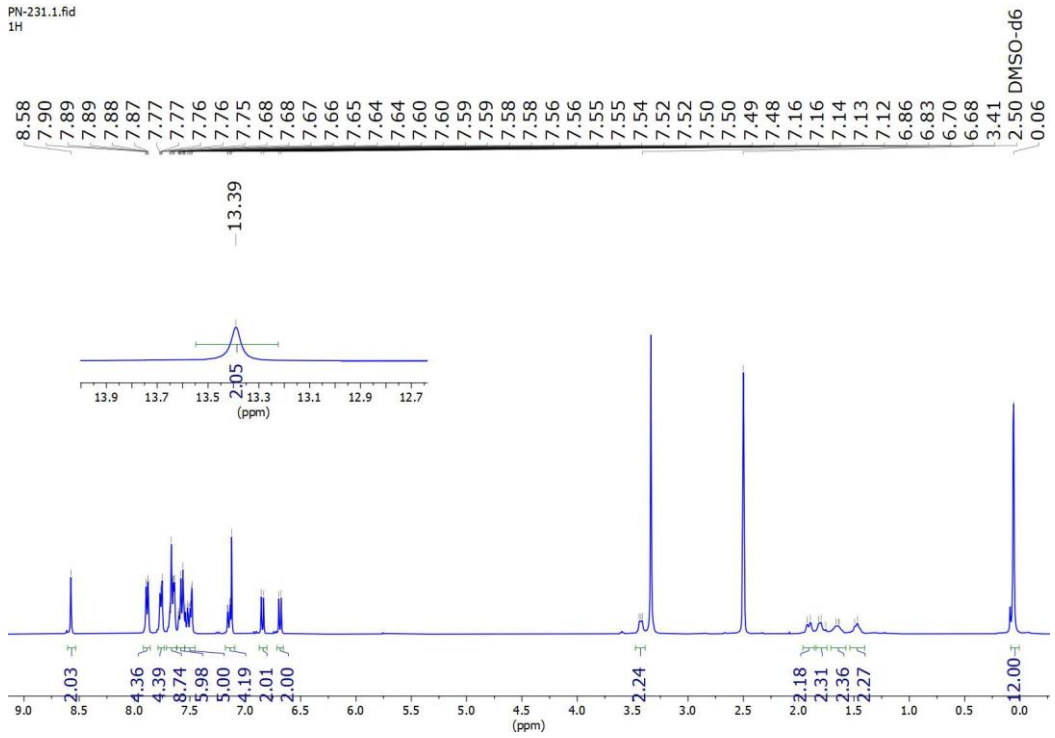

Figure S16: [1]H-NMR of compound **TPZBSA** in DMSO-d_6

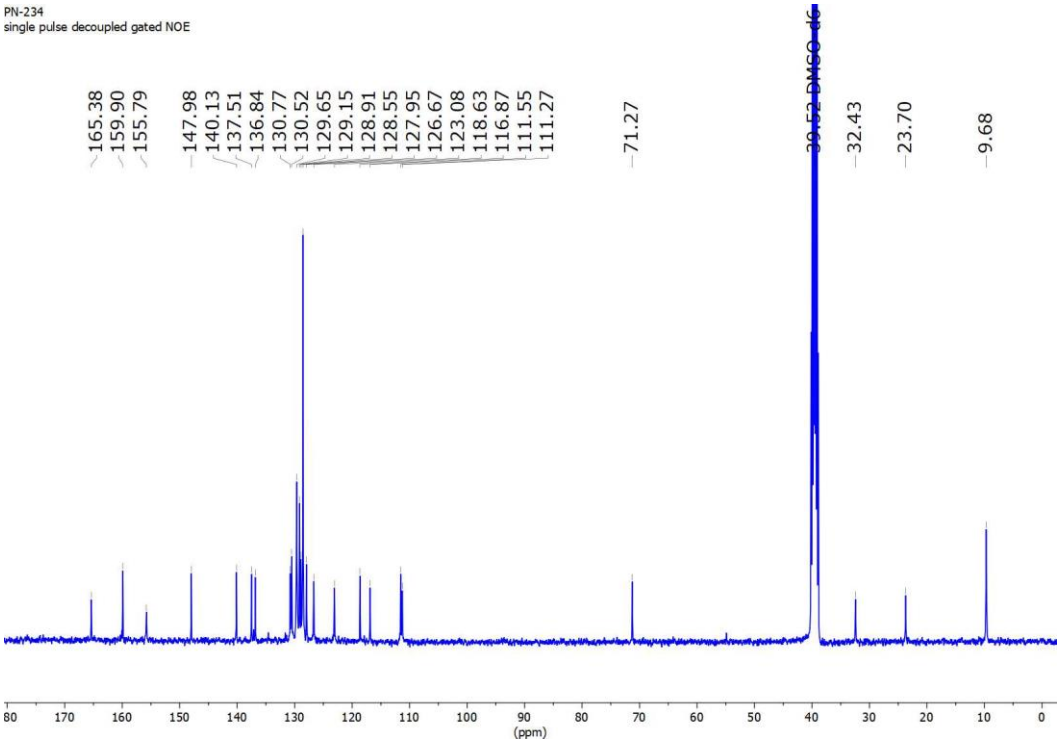

Figure S17: [13]C-NMR of compound **TPZBSA** in DMSO-d_6

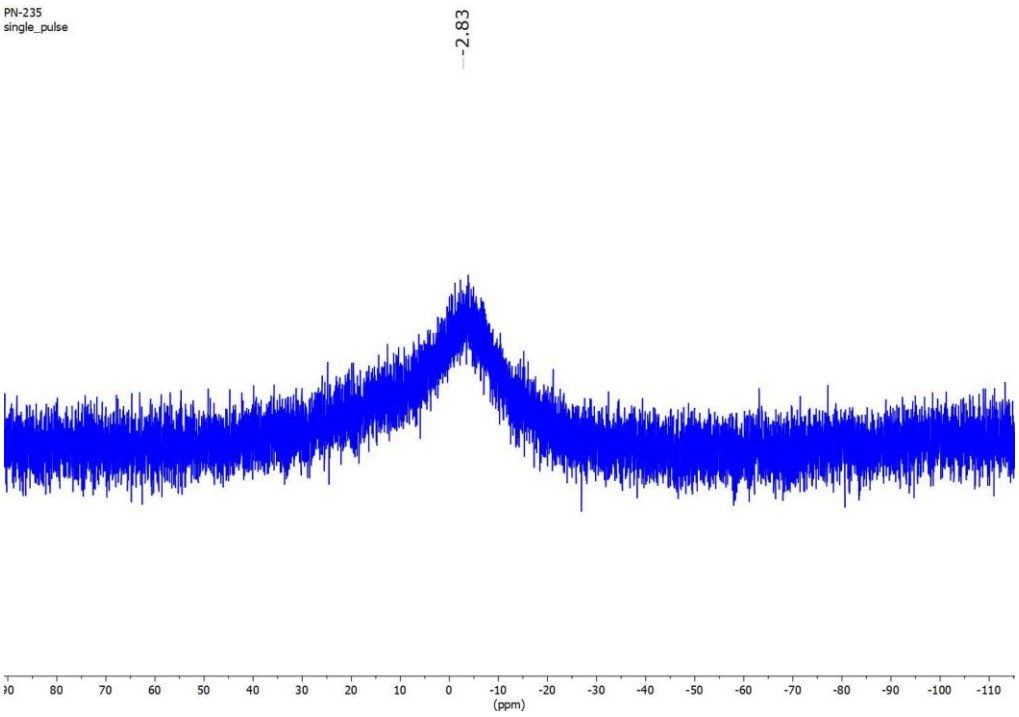

Figure S18: ^{11}B-NMR of compound **TPZBSA** in DMSO-d_6

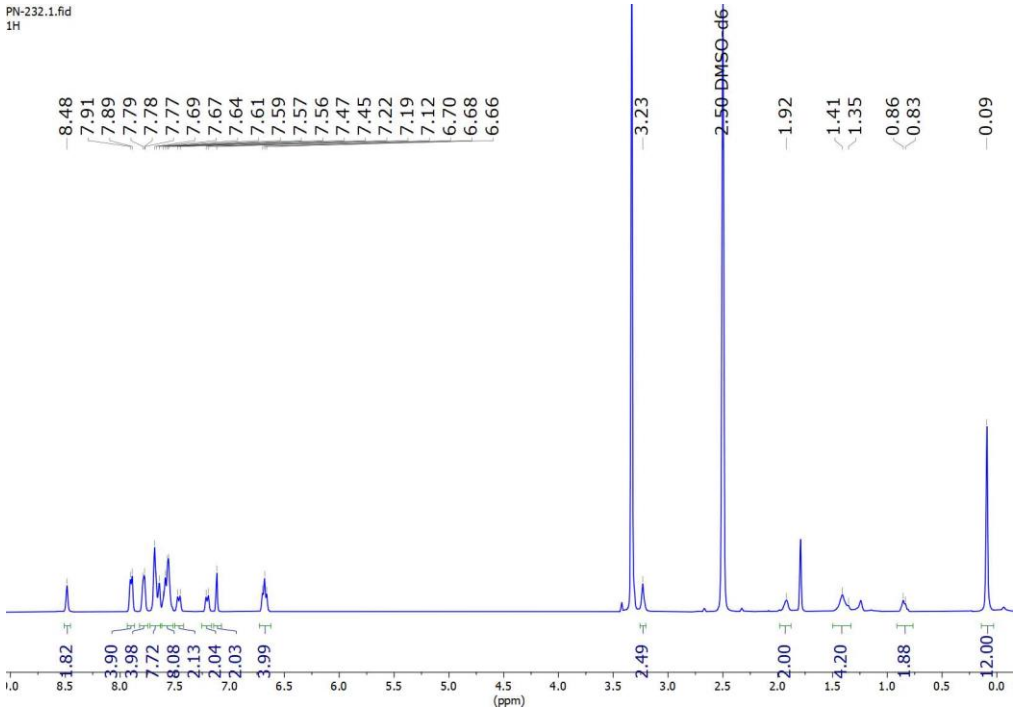

Figure S19: ^{1}H-NMR of complex **TPZBSA-Zn** in DMSO-d_6

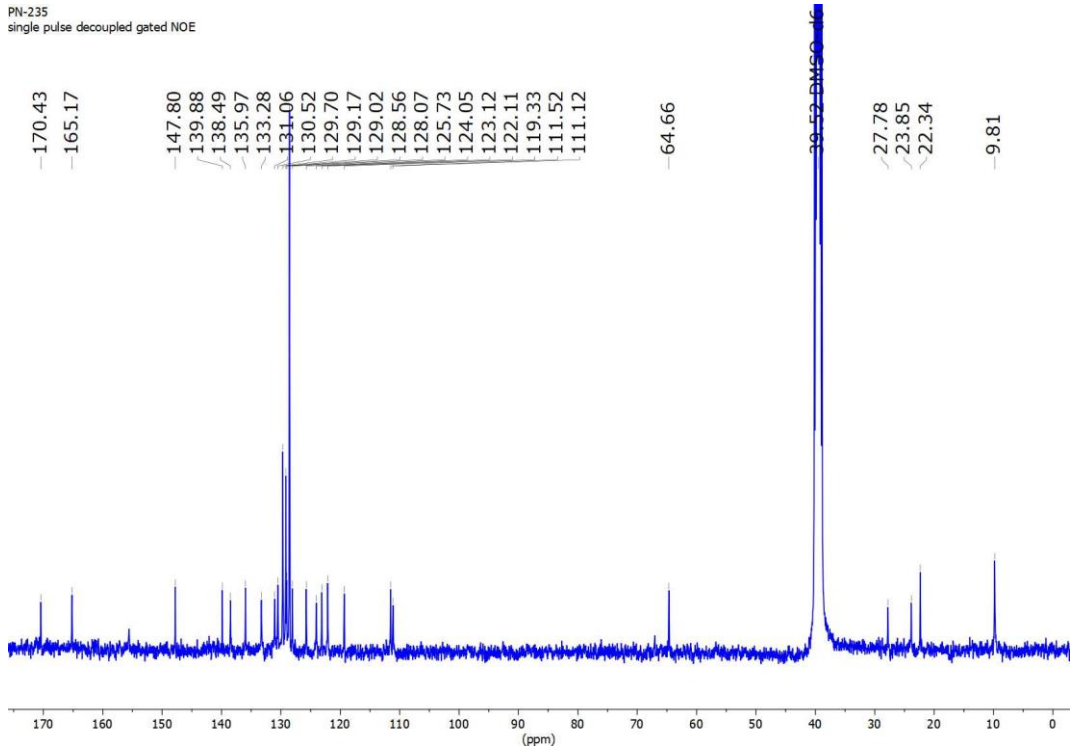

Figure S20: ^{13}C-NMR of complex **TPZBSA-Zn** in DMSO-d_6

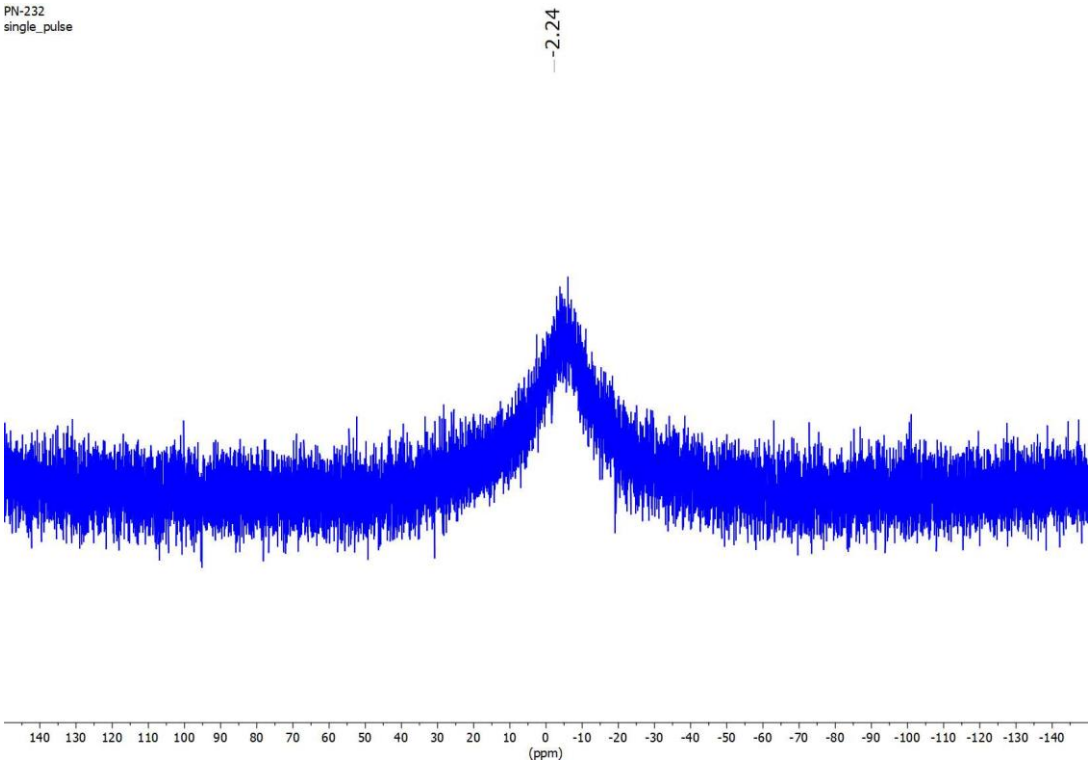

Figure S21: ^{11}B-NMR of complex **TPZBSA-Zn** in DMSO-d_6

6. References

[1] Y. Chen, Y. Tang, P. Li, Y. Wang, Y. Zhuang, S. Sun, D. Wang, W. Wei, *Anal. Chim. Acta* 2023, **1278**, 341739.

[2] A. M. Fekry, S. M. Azab, M. Shehata, M. A. Ameer, *RSC Adv.* 2015, **5**, 51662-51671.

[3] Y. Jing, E. Lin, X. Su, Y. Liu, H. Li, X. Yuan, L. Ping and Y. Fan, *Sci. Rep.*, 2016, **6**, 29230.

[4] T. Leelasree, S. Goel and H. Aggarwal, *ACS Appl. Nano Mater.*, 2022, **5**, 16753–16759.

[5] Z. Huang, Z. Li, L. Xu, C. Wei, C. Zhu, H. Deng, H. Peng, X. Xia and W. Chen, *Anal. Chem.*, 2020, **92**, 11438–11443.

[6] J. Zhang, J. Liu, X. Su, Y. Wang and L. Chen, *Electrochem. Commun.*, 2009, **11**, 733–735.

[7] D. Rani, K. K. Bhasin and M. Singh, *ACS Mater. Lett.*, 2020, **2**, 9–14.

[8] Z. O. Erdogan, H. Balci, *Spectrochim. Acta A Mol. Biomol. Spectrosc.* 2023, **285**, 121853.

[9] S. H. Hashemi, F. Keykha, *Anal. Methods* 2019, **11**, 5405-5412.

[10]]R. Jerome, A. K. Sundramoorthy, *Anal. Chim. Acta* 2020, **1132,** 110-120.

[11] T. I. Sebokolodi, D. S. Sipuka, C. Muzenda, O. V. Nkwachukwu, D. Nkosi, O. A. Arotiba, *Chemosphere* 2022, **303**, 134961.

[12] G. Sridharan, K. L. Babu, D. Ganapathy, R. Atchudan, S. Arya, A. K. Sundramoorthy, *Crystals*, 2023, **13,** 589.

[13] K. R. Tambwekar, R. B. Kakariya, S. Garg, *J. Phar. Biomed. Anal.* 2003, **32**, 441-450.